

# A STUDY OF DIFFERENT MESH GENERATION APPROACHES TO CAPTURE AERODYNAMIC COEFFICIENTS FOR HIGH-LIFT CONFIGURATIONS

**Alexandre P. Antunes<sup>\*</sup>, Ricardo Galdino da Silva<sup>†</sup>, João Luiz F. Azevedo<sup>‡</sup>**

**<sup>\*</sup> Instituto Tecnológico de Aeronáutica, ITA**

**<sup>†</sup> Universidade de São Paulo, USP**

**<sup>‡</sup> Instituto de Aeronáutica e Espaço, CTA/IAE/ALA**

**Keywords:** *Computational Fluid Dynamics, High-Lift Devices, Aerodynamic Design*

## Abstract

*The paper presents three-dimensional simulations over a trapezoidal wing with a single slotted flap and a slat, which was a model developed in order to provide a database for CFD validation. This semi-span model has been tested both in the NASA Ames 12-Foot Pressurized Tunnel (PWT) and the NASA Langley 14 by 22 Foot Subsonic Wind Tunnel (SWT). The simulations are performed for two flaps deflections, 20 and 25 degrees, and a few angles of attack; the slat deflection is hold constant at 30 degrees. Different mesh methodologies such as hexahedral meshes, and hybrid prismatic-tetrahedral meshes are used to perform the numerical simulations. In order to observe the accuracy of the obtained aerodynamic coefficients, with respect to mesh refinement, a small number of simulations is performed with finner meshes. The baseline grids range from 7.2 million to 12.8 million cells, while the finner grids are around 23 million cells.*

## 1 Introduction

Computational Fluid Dynamics (CFD) has been consolidated as a quite mature science along the last thirty years of development [1, 2]. Nowadays, CFD is a well-know technology, deeply inserted into aerodynamic groups to perform the most diverse types of analyses. The paper will present three-dimensional simulations over

a trapezoidal wing with a single slotted flap and a slat [3, 4]. The model was developed in order to provide a database for CFD validation [5]. The simulations are performed for two flaps deflections, 20 and 25 degrees, and a few angles of attack; the slat deflection is hold constant at 30 degrees. Different mesh methodologies such as hexahedral meshes, and hybrid prismatic-tetrahedral meshes are used to perform the numerical simulations. In order to observe the accuracy of the obtained aerodynamic coefficients, with respect to mesh refinement subject, a small number of simulations is accomplished with finner meshes. The generated baseline grids range from 7.2 million to 12.8 million cells, while the finner generated grids are around 23 million cells for both methodologies.

The high-lift devices are intrinsically complex lifting components, that generate flow patterns with a vast range of physical phenomena [6, 7, 8]. On such devices, one can commonly find boundary layer confluence, sonic regions, detached regions, flow relaminarization, among other phenomena. The capability to numerically capture all these physical phenomena provides confidence on the obtained aerodynamic coefficients. This accuracy is a very important subject during the definitions of the high-lift systems due to the target design requirements that must be achieved to avoid penalties on the airplane performance [9, 10]. Hence, to achieve the target de-

sign requirements, a combination of several sets of leading-edge and trailing-edge high-lift systems can be used. For the leading-edge, one can choose which device is more appropriate among the following possibilities: hinged leading edge, variable camber leading edge, fixed slot, simple Krueger flap, folding, bull-nose Krueger flap, two-position slat, three-position slat. In a similar fashion, a large amount of possibilities is available for the trailing-edge devices, for instance: split flap, plain flap, simple slotted flap, fixed vane/main double slotted flap, main/aft double-slotted flap, triple-slotted flap. The combination of each one of these devices leads to different weight, cost, reliability, fairing drag, and fairing blockage, thus, resulting in different stall characteristics. From the fifties' to the seventies', the increase in the complexity of high-lift devices was the tendency [11]. However, in the late seventies', the beginning of CFD use allowed a way to decrease the high-lift device complexity by means of shape and gap/overlap optimization. The accurate simulations over high-lift configurations is the cutting edge technology to generate simpler high-lift devices and decrease the number of wind tunnel campaigns. Figure 1 and 2 show some representative numerical simulations performed for a commercial airplane. As one can observe in these figures, the relevant features of the high-lift system of a commercial airliner have been represented in the simulations. The calculations in Fig. 1 have considered the wing-body configuration, with high-lift devices extended, and the pylon and nacelle (WBPZ). Results in Fig. 2 were obtained for the wing-body with high-lift devices (WBZ) only.

A comparison of the results for these simulations is presented in Fig. 3, which shows the aircraft lift coefficient ( $C_L$ ) as a function of angle-of-attack obtained by the CFD calculations, for the WBPZ and the wind tunnel results. One can see from Fig. 3 that a reasonable adherence between the wind tunnel results and the numerical simulation was obtained, at least in terms of lift coefficients. Unfortunately, the results for the drag coefficient,  $C_D$ , were not as encouraging as those for  $C_L$  [12]. For this reason, a simpler trapezoidal

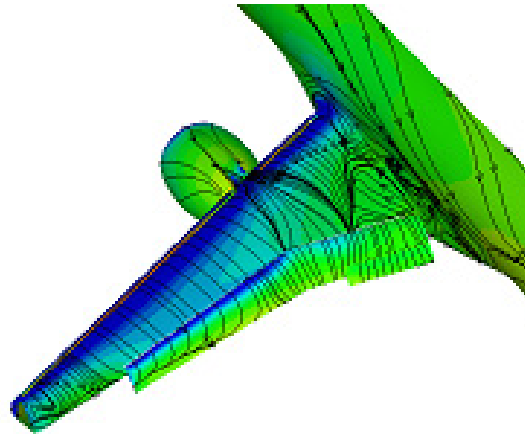


**Fig. 1** Flow pattern over the wing of a commercial aircraft for the WBPZ configuration.

wing with high-lift devices is taken as the main subject of study in the present work. This configuration is also publicly available and, hence, this facilitates the reporting of the present results. As previously discussed, the main objective of the investigation is to be able to generate guidelines for the accurate calculation of drag coefficients for commercial airliner configurations with high-lift devices extended.

## 2 Trapezoidal Wing Model with Body Pod

A trapezoidal wing model has been tested both in the NASA Ames 12-Foot Pressurized Tunnel (PWT) and the NASA Langley 14 by 22 Foot

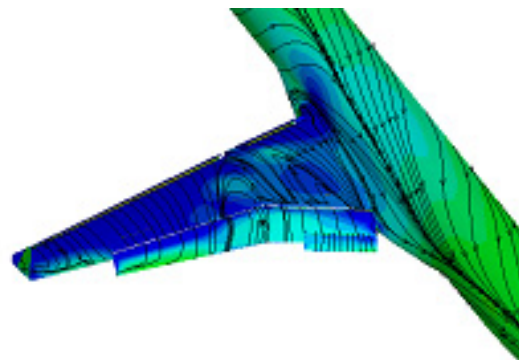


**Fig. 2** Flow pattern over the wing of a commercial aircraft for the WBZ configuration.

# A STUDY OF DIFFERENT MESH GENERATION APPROACHES TO CAPTURE AERODYNAMIC COEFFICIENTS FOR HIGH-LIFT CONFIGURATIONS

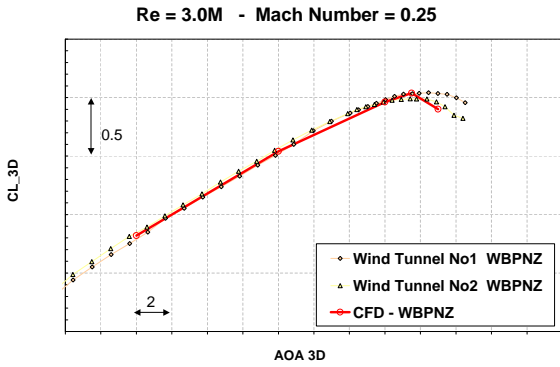


**Fig. 3** CL versus AOA curve for configuration WBPNZ.

Subsonic Wind Tunnel (SWT) as part of the Advanced Subsonic Technology (AST) High-Lift Program, and the Advanced Subsonic Technology (AST) Airframe Noise Program. A considerably large number of high-lift device configurations and deflections was tested to produce the necessary experimental data for validation and development of CFD methods. Figure 4 shows some geometrical details from one of the tested configurations.

Three different configurations are adopted in order to perform the present study, one with a partial span flap and the others with a full span flap. These selected configurations are identified as *one*, *eight* and *nine*, according to the definition of the NASA configuration control matrix. The slat and flap deflections, for the above mentioned configurations, are respectively described below. For further details about the gap/overlap, the interested reader is directed to Ref. [3].

- Full Span Flap - Slat 30° and Flap 25°;
- Full Span Flap - Slat 30° and Flap 20°;
- Partial Span Flap - Slat 30° and Flap 25°.

In order to perform the first set of simulations, hybrid tetrahedral/prismatic meshes were generated over the adopted configurations. The generated meshes have a spherical outside boundary, which is located fifty chords away from the model. Since no wall boundary condition is imposed on the outer boundary, it is not necessary



**Fig. 4** Trapezoidal wing in the wind tunnel test section.

to reproduce in detail the wind tunnel test section. At this outer boundary of the mesh, the characteristic equations are imposed as boundary conditions. At mesh symmetry plane, the symmetry boundary condition is imposed. It worth to mention that the experimental results are corrected to eliminate the effect of the tunnel wall boundary layer over the aerodynamic coefficients of the configuration. Thus, the application of the above mentioned boundary conditions are appropriate for the performed simulations.

The hybrid baseline meshes, for the three configurations, have 9.8 million, 7.3 million, and 12.8 million cells, respectively. In Fig. 5, one can see the baseline surface meshes for configurations *one* and *nine*. The prismatic mesh layer is generated over the model surface using a geometric law with a growth ratio of 1.15. Moreover, the  $Y_{plus}$  is set equal to one, by adjustments on the distance of the first point outside the wall. This distance is defined based on the flight condition and the expected shear stress on the surface.

In particular, the generated hybrid baseline meshes have in common the fact that, at the trailing edge, there is only one cell face. In order to observe the effect of the trailing edge refinement on the obtained aerodynamic coefficients, mainly in the  $C_D$  coefficient, a refined mesh was generated over configuration *nine*. In this case, the trailing edge of the configuration *nine* is rep-

resented by three cell faces instead of just one. Although it seems a small change, the overall size of the mesh greatly increases. It goes from 12.8 million cells to 22.3 million cells.

Another set of simulations is performed using the hexahedral mesh methodology. Here, the main objective is to perform comparisons between the aerodynamic coefficients obtained by the hexahedral mesh and those obtained by the hybrid mesh. In order to accomplish the necessary simulations for the mesh methodology comparisons, two hexahedral meshes are generated over configuration *one*. The first one with 12 million cells, and the second one with 22.8 million cells. One can see in Fig. 6 the less refined hexahedral mesh. In both cases the mesh distribution along the direction normal to the surface follows a geometric law, with a growth ratio of 1.15. The first point outside the wall is also adjusted to have a  $Y_{plus}$  of one. Figure 7 shows a station cut over the less refined hexahedral mesh at the mid-station in the spanwise direction of the model wing.

The comparison of results obtained with hexahedral and tetrahedral/prismatic meshes can provide some insight on the required mesh size for the hybrid and the hexahedral methodologies in order to better capture the aerodynamic coefficients.

### 3 Results

The numerical simulations for all the analyzed cases were performed using the CFD++ solver [13] with the Spalart-Allmaras [14] turbulence model. In the present case, only the test conditions adopted at the NASA Langley 14 by 22 Foot Subsonic Wind Tunnel (SWT) are used to perform the numerical simulations. These conditions are Mach number of 0.20 and Reynolds number of 4.3 million, based on the model mean aerodynamic chord.

#### 3.1 Configuration One

In Fig. 8, one can see the  $AOA$  versus  $C_L$  curve obtained for configuration *one* with the hybrid

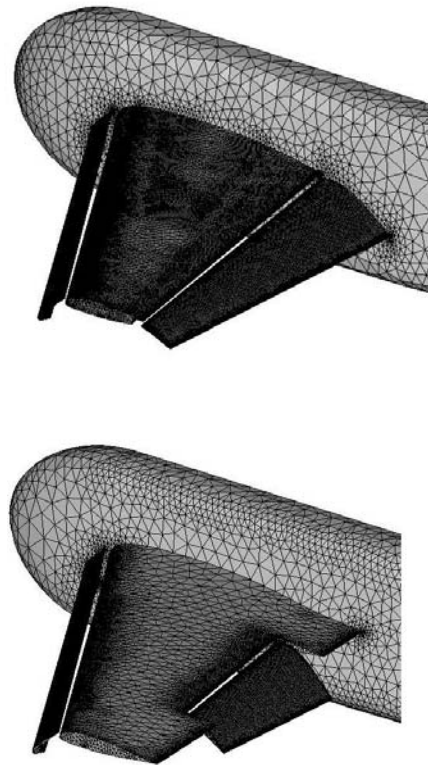


**Fig. 5** Surface mesh for configuration *one* and *eight* (Hybrid Mesh).

and the hexahedral meshes. The somewhat large differences observed between the computational results and the experimental  $C_L$  coefficients were not expected. In Fig. 8, one can observe the shift in the  $C_{L0}$  coefficient for both mesh methodologies. Moreover, the hybrid mesh presented a premature stall angle of attack and a lower  $C_L$  value



**Fig. 6** Surface mesh for configuration *one* (Hexahedral Mesh).

## A STUDY OF DIFFERENT MESH GENERATION APPROACHES TO CAPTURE AERODYNAMIC COEFFICIENTS FOR HIGH-LIFT CONFIGURATIONS

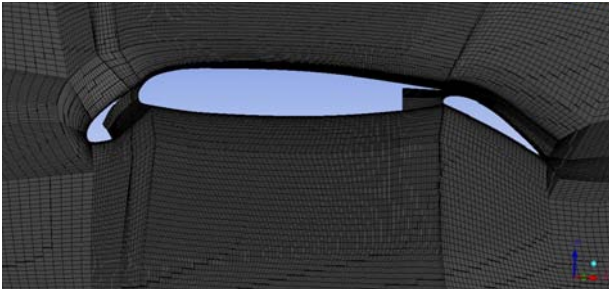


**Fig. 7** A station cut over the less refined hexahedral mesh.

at the stall angle. On the other hand, the hexahedral mesh was able to capture the stall angle of attack. However, the obtained  $C_{L_{max}}$  is also underpredicted.

The obtained  $C_L$  values for the hexahedral baseline and refined meshes are closer to the experimental results than those obtained by the hybrid mesh. The aerodynamic coefficients calculated in the hexahedral meshes, baseline and refined meshes, have very small differences. Such differences do not exceed 0.04 in terms of the  $C_L$  coefficient. Furthermore, such maximum differences are only observed at higher angles of attack considered in the present investigation. Typically, at higher angles of attack, the nonlinearities of the flowfield are more pronounced and refined meshes are more adequate to better capture such nonlinearities. The present results, therefore, show that the hexahedral baseline mesh is already adequate for the intended simulations in the present case.

In terms of drag coefficient comparisons, one can see in Fig. 9 a mismatch of the hybrid mesh results with respect to the experimental results. The difference starts at 80 drag counts at  $C_L$  of 1.60 and reaches 450 drag counts near  $C_L$  of 2.70. Usually, the drag coefficient associated to the pressure component has a significant contribution on the overall computation of the total drag. The pressure drag contribution is typically negative at the trailing edge and, since the hybrid mesh only has one cell element along the trailing edge, it is quite possible that  $C_D$  is being overpredicted in the hybrid mesh calculations for this case. The results obtained with the hexahe-

dral meshes, once again, show a better adherence to those from the experimental data. Nevertheless, near the stall angle of attack, one can see a small difference in  $C_D$  in Fig. 9, which is probably caused by the fact that the  $C_L$  values were slightly underpredicted at the stall condition. The explanation, at the present time, that such differences in the hexahedral mesh calculations come about because the current calculations are indicating more flow separation, at the flight condition in question, than the actual experiments. Hence, one would have less  $C_L$ , but more  $C_D$ .

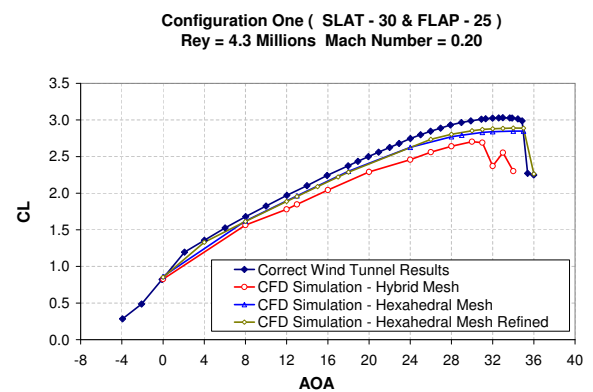


**Fig. 8** AOA versus  $C_L$  for the configuration one.

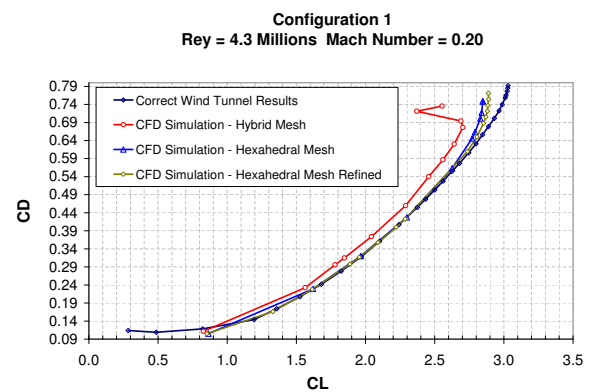


**Fig. 9**  $C_L$  versus  $C_D$  for the configuration one.

Figure 10 shows an isometric view of the shear lines at different angles of attack for configuration one. It can be noticed that, at zero angle of attack, the flow pattern obtained with both baseline hexahedral and hybrid meshes is pretty

similar. There is a massive separated region over the flap upper surface, as well as a vortex region at the flap trailing edge near the pod junction. At lower angles of attack, it is very common to have this separated flow region over the high-lift devices.

As the angle of attack increases, the flow-field pattern captured by both mesh methodologies become considerably different. The hexahedral mesh shows a constant separated flow region on the flap-pod junction, for angles of attack up to 28 deg. On the other hand, the results obtained with the hybrid mesh show that the flap-pod separated region disappears at angles of attack higher than 8 deg. Moreover, the hybrid mesh shows a separated flow area on the pod element, which is not present in the hexahedral mesh. Hence, one can notice how different the obtained results can be as a function of the adopted mesh methodologies and the spatial discretization.

Part of this discrepancy can be attributed to the horseshoe vortex present at the region near the leading edge of the slat, as one can see in Fig. 11. Usually, whenever a surface is mounted into another base surface with a substantial angle between them, such as the slat and the pod surfaces, it is possible to have the appearance of such vortical structures. This vorticity affects the upstream flowfield, the downstream flowfield and the shear lines over the body. Moreover, it makes the accurate capture of the aerodynamic coefficients a challenging task. Since the hexahedral mesh has a more refined volumetric discretization, it can better capture the emanated vorticity from the upstream flowfield. In the hybrid mesh, the tetrahedra located beyond the prism layer present a rapid volumetric growth, which may cause some adverse effects in the capability of capturing such physical phenomena with accuracy.

### 3.2 Configuration Eight

The simulations performed for configuration *eight* used only the hybrid baseline mesh. In Fig. 12, one can observe the  $AOA$  versus  $C_L$  curve obtained from the simulations. The wind tunnel results do not contain corrected data information

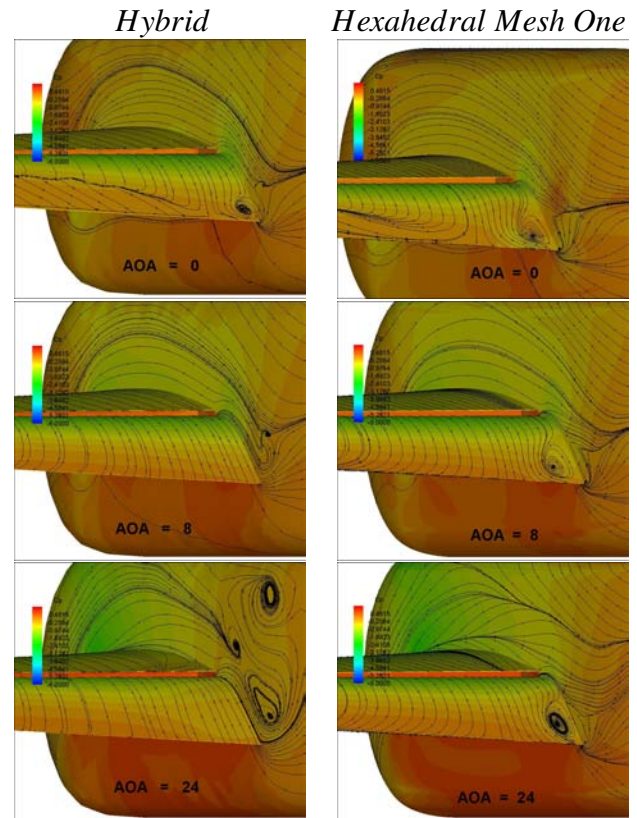


**Fig. 10** Shear lines over configuration *one* for three angles of attack.

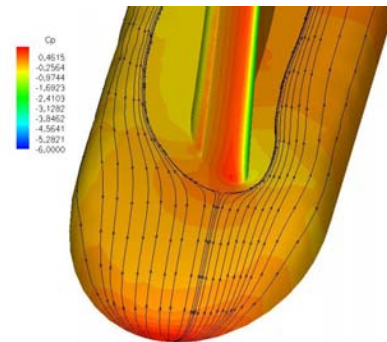


**Fig. 11** Horseshoe vortex emitted from the slat leading edge region.

up to the stall angle of attack. For this reason, one cannot observe the experimental results at the stall angle of attack.

One can notice that there is a discrepancy in relation to the experimental results, in a very similar way as observed for the hybrid mesh calculations for configuration *one*. This difference is less pronounced due to the lower flap deflection in the present case. Lower flap deflections generate

# A STUDY OF DIFFERENT MESH GENERATION APPROACHES TO CAPTURE AERODYNAMIC COEFFICIENTS FOR HIGH-LIFT CONFIGURATIONS

smaller aerodynamic spanwise loading. Thus, the vortex near the slat leading edge has a lower circulation intensity. If the discrepancies can be attributed to the inability of accurately capturing the effect of this vortex, as it was stated, the decrease in this structure intensity leads to a less disturbed downstream flowfield. Therefore, the simulation can better capture the aerodynamic coefficients.

In Fig. 13, one can see the  $C_D$  versus  $C_L$  curve. Here, one can notice that the same shift, observed for configuration *one*, is also present. In Fig. 14, one can observe the shear lines for this configuration at two different angles of attack, 12 and 16 deg. The flow pattern follows the same behavior observed for configuration *one*. Near the flap-pod junction, there is a separated flow region, that disappears at higher angles of attack. Therefore, for this configuration, flow separation only disappears at 16 deg, whereas for configuration *one* it disappears at 8 deg. angle of attack.

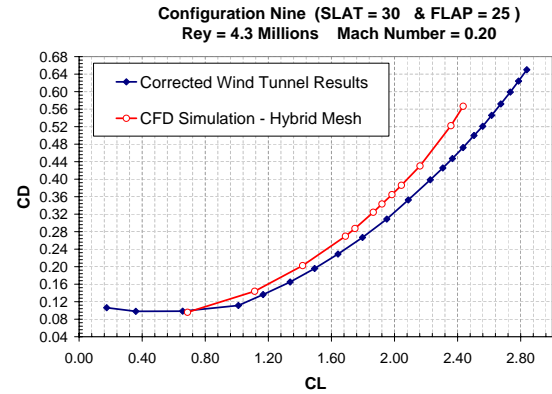


Fig. 13 CL versus CD for configuration *eight*.

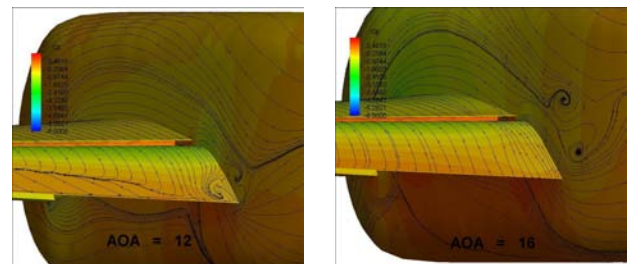


Fig. 14 Shear lines over configuration *eight* for two angles of attack.

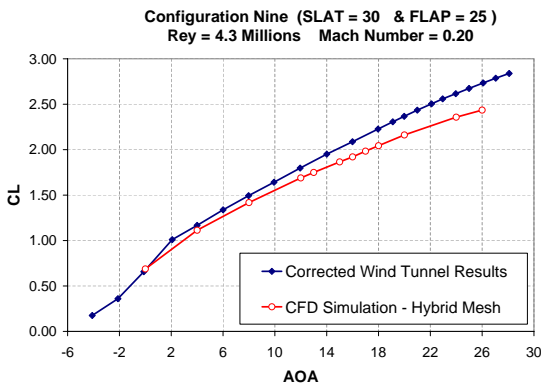


Fig. 12 AOA versus CL for configuration *eight*.

### 3.3 Configuration Nine

The simulations performed for this configuration used the baseline and the refined hybrid meshes. In Fig. 15, one can observe the shear lines for the baseline mesh of configuration *nine* at the following angles of attack, 0, 8, 20, and 28 deg. There is an important aspect that must be pointed out from Fig. 15, and which is the appearance of a small separated region on the wing trailing edge near the wing-pod junction, at angle of attack of 8 deg. This separated region might be generated by

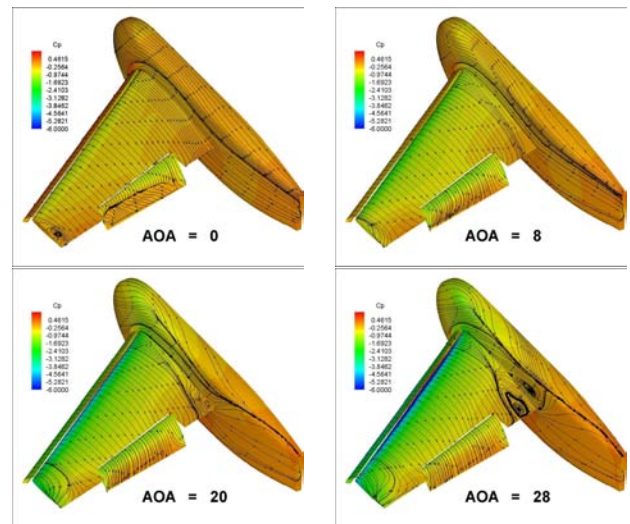


Fig. 15 Shear lines over the configuration *nine* for four angles of attack using the baseline mesh.

the adverse pressure gradient at the trailing edge, as well as by an adverse effect caused by the upstream vorticity emanated from the slat leading edge. This small separated region propagates upstream as the angle of attack increases.

In Fig. 16, one can observe the  $AOA$  versus  $C_L$  curve. A good adherence is obtained until 12 deg. angle of attack for both meshes. Beyond this angle of attack, there is a mismatch between the numerical and the experimental results. Again, the discrepancy can be attributed to the inability of the present calculation procedure, with the meshes here used, of capturing with adequate accuracy the effect of the emanated vorticity from the slat leading edge. An interesting point here is the fact that, at lower angles of attack, a good matching between the experimental and the numerical coefficients is obtained, for all the three configurations, despite the separated regions over the high-lift devices.

It is also possible that, at lower angles of attack, the vorticity from the slat leading edge is being convected towards the lower surface of the model and, therefore, not disturbing the upper surface. At the lower surface, usually, there is no adverse pressure gradient, thus, the presence of the upstream vorticity might cause boundary layer thickening, and an increase in the  $C_D$  but not a separation of the flow. It should be pointed out, however, that the upper surface of the flap is always separated for such angles of attack. On the other hand, for the higher  $AOA$ , the upstream vorticity disturbs the flowfield on the upper surface, causing boundary layer thickening and distortion of the shear lines due to the low pressure core of the vortex. In this condition, the accurate capture of the aerodynamic coefficient is difficult.

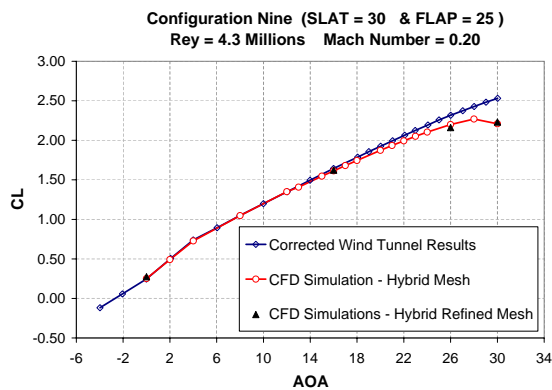


Fig. 16  $CL$  versus  $AOA$  for configuration *nine*.

The obtained results for the refined mesh did not produce any improvement in the calculated  $C_L$  coefficients. Although this mesh has more cells than the baseline mesh, mostly of the refinement is concentrated in the trailing edge of the wing. Hence, in terms of volumetric aspect, this mesh does not provide a better capability to capture the horseshoe vortex. Figure 17 shows a comparison in terms of drag coefficients between the numerical and the experimental results. It can be noticed that the shift is smaller than the observed for configurations *one* and *eight* for both simulations, *i.e.*, with the baseline and the refined meshes. The refined mesh does not present a better matching with the experimental results even for  $C_D$ , despite the fact that most of the refinement happened at the trailing edge. This is an indication that, although the mesh is more adequate to capture the pressure drag component at the trailing edge, the lack of a volumetric refinement does not allow the capture of the effect of the horseshoe vortex. Hence, the overall results are not improved.

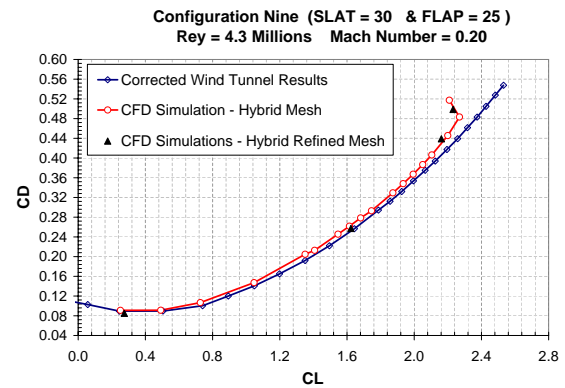


Fig. 17  $CL$  versus  $AOA$  for configuration *nine*.

## 4 Conclusions

The performed simulations for all the three configurations have shown a fairly good correlation with the experimental results up to the stall angle of attack. Nevertheless, the matching is not perfect and some discrepancies are readily observed in the results presented. The hexahe-

## A STUDY OF DIFFERENT MESH GENERATION APPROACHES TO CAPTURE AERODYNAMIC COEFFICIENTS FOR HIGH-LIFT CONFIGURATIONS

dral mesh methodology, adopted for configuration *one*, has shown that this approach produces better results than those obtained with the hybrid mesh methodology. This conclusion is correct for both aerodynamic coefficients,  $C_L$  and  $C_D$ . In general, the hexahedral mesh methodology provides meshes with a lower number of cells and with a better volumetric discretization. In the authors' opinion, in order to have a hybrid mesh with the same accuracy of the hexahedral mesh, the number of elements in the hybrid mesh would need to be increased at least by a factor of 2.

The results obtained with the configuration *nine* are closer to the experimental data, although the used mesh for the simulation is not hexahedral. This is possible because for this configuration the horseshoe vortex is less intense, since the flap is not extended to the wing-pod junction. The horseshoe vortex turns the capture of the aerodynamic coefficients a challenging task. In such case, a careful evaluation of the mesh characteristics is necessary. There is the need for developing very controlled meshes, in terms of point distributions and mesh spacings, and, also, mesh topologies which adequately allow capturing of the phenomena expected in the simulations.

### Acknowledgments

The authors acknowledge the partial support of Conselho Nacional de Desenvolvimento Científico e Tecnológico, CNPq, under the Research Project Grant No. 312064/2006-3.

### References

- [1] Johnson, T.F., and Tinoco, E.N., "Thirty Years Of Development and Application Of CFD at Boeing Commercial Airplane Seattle," *Computers & Fluids*, Vol. 34, No. 10, Dec. 2005, pp. 1115-1151.
- [2] Vos, J.B., Rizzi, A., Darraq, D., and Hirschel, E.H., "Navier-Stokes Solvers in European Aircraft Design," *Progress in Aerospace Sciences*, Vol. 38, No. 08, Nov. 2002, pp. 601-697.
- [3] <http://db-www.larc.nasa.gov/trapwing/archieve/register/> [visited 20 Dec. 2009]
- [4] Chaffin, M., and Pirzadeh, S., "Unstructured Navier-Stokes High-Lift Computations on a Trapezoidal Wing," AIAA Paper No. 2005-5084, *23rd AIAA Applied Aerodynamics Conference*, Toronto, Canada, Jun. 2005.
- [5] Johnson, P., Jones, K.M., and Madson, M., "Experimental Investigation of a Simplified 3D High-Lift Configuration in Support of CFD Validation," AIAA Paper 2000-4217, *18th AIAA Applied Aerodynamics Conference and Exhibit*, Denver, CO, Aug. 2000.
- [6] van Dam, C.P., "The Aerodynamic Design of Multi-Element High-Lift Systems for Transport Airplanes," *Progress in Aerospace Sciences*, Vol. 38, No. 2, Feb. 2002, pp. 101-114.
- [7] Payne, F.M., Wyatt, G.W., Bogue, D.R., and Stone, R.C., "High Reynolds Number Studies of a Boeing 777-200 High-Lift Configuration in The NASA ARC 12' Pressure Tunnel and NASA LaRC National Transonic Facility," AIAA Paper 2000-4220, *18th AIAA Applied Aerodynamics Conference and Exhibit*, Denver, CO, Aug. 2000.
- [8] Rogers, S.E., Roth, K., Nash, S.M., Baker, M.D., Slotnick, J.P., Whitlock, M., "Computational of Viscous Flow for a Boeing 777 Aircraft in Landing Configuration," AIAA Paper No. 2000-4221, *18th AIAA Applied Aerodynamics Conference and Exhibit*, Denver, CO, Aug. 2000.
- [9] Eliasson, P., "CFD Improvements for High-Lift Flows in the European Project EUROLIFT," AIAA Paper No. 2003-3795, *21st AIAA Applied Aerodynamics Conference*, Orlando, FL, Jun. 2003.
- [10] Rudnick, R., "CFD Assessment for High-Lift Flows in the European Project EUROLIFT," AIAA Paper No. 2003-3794, *21st AIAA Applied Aerodynamics Conference*, Orlando, FL, Jun. 2003.
- [11] Flaig, A., and Hilbig, R., "High-Lift Design for Large Civil Aircraft," *High-Lift Systems Aerodynamics*, AGARD CP-515, Sept. 1993, pp. 31-1-31-12.
- [12] Rumsey, C.L., and Rivers, S.M., "Study of CFD Variation on Transport Configurations from the Second Drag-Prediction Workshop," *Progress in Aerospace Sciences*, Vol. 34, No. 07, Aug.

2005, pp. 785-816.

- [13] Metacomp Technologies Inc., CFD++, <http://www.metacomptech.com/>.
- [14] Spalart, P.R., and Allmaras, S.R., “A One-Equation Turbulence Model for Aerodynamic Flows,” AIAA Paper No. 92-0439, *Proceedings of the 30th AIAA Aerospace Sciences Meeting and Exhibit*, Reno, NV, Jan. 1992.
- [15] Ansys Inc., ICEM-CFD<sup>™</sup>, <http://www.icemcfd.com/>.

### Copyright Statement

The authors confirm that they, and/or their company or organization, hold copyright on all of the original material included in this paper. The authors also confirm that they have obtained permission, from the copyright holder of any third party material included in this paper, to publish it as part of their paper. The authors confirm that they give permission, or have obtained permission from the copyright holder of this paper, for the publication and distribution of this paper as part of the ICAS2010 proceedings or as individual off-prints from the proceedings.